

Accepted for publication in Polymer Composites
Published in May, 2015
DOI: 10.1002/pc.23006

Toughening Linear Low-Density Polyethylene With Halloysite Nanotubes

D. Pedrazzoli ^(a), A. Pegoretti ^(a)*, R. Thomann ^(b),
J. Kristóf ^(c), J. Karger-Kocsis ^(d,e)

^(a) University of Trento, Department of Industrial Engineering and INSTM Research Unit, Via Mesiano 77, 38123 Trento (Italy)

^(b) Albert-Ludwigs-Universität Freiburg, Institut für Makromolekulare Chemie und Freiburger Materialforschungszentrum, Stefan-Meier-Str. 31, 79104 Freiburg (Germany)

^(c) Department of Analytical Chemistry at the University of Pannonia, 8200 Veszprém (Hungary)

^(d) Budapest University of Technology and Economics, Faculty of Mechanical Engineering, Department of Polymer Engineering, 1111 Budapest (Hungary)

^(e) MTA–BME Research Group for Composite Science and Technology, Műegyetem rkp. 3, 1111 Budapest (Hungary)

*Corresponding author.

Tel.: +39-0461-282452; fax: +39-0461-281977

e-mail address: alessandro.pegoretti@unitn.it (A. Pegoretti)

Abstract

Linear low density polyethylene (LLDPE) based composites were prepared through melt compounding and hot pressing using both untreated and treated halloysite nanotubes (HNT) up to filler contents of 8 wt% in order to assess the role of the filler exfoliation and surface treatment on the thermal, mechanical and rheological properties of the resulting composites.

The addition of treated nanoparticles resulted in a better dispersion of the filler within the matrix, as confirmed by observations conducted at scanning and transmission electron microscopies. An interesting decrease in both complex viscosity and shear storage modulus was recorded for all LLDPE-HNT nanocomposites in their melts.

Through differential scanning calorimetry runs it was found that HNT addition produced an increase of the crystallization peak temperature, while thermogravimetric analyses showed a remarkable improvement of the thermal stability with the nanofiller content. The addition of treated HNT nanoparticles produced better improvements in elastic modulus and tensile properties at break without loss in ductility than untreated ones.

The fracture toughness, evaluated by the essential work of fracture (EWF) approach, showed significant improvement with addition of treated HNT. Incorporation of untreated HNT produced an adverse effect on the fracture toughness when considering the related nanocomposite filled with 8 wt% HNT.

Both creep tests and dynamic mechanical analyses showed an overall enhancement of mechanical properties due to addition of HNT, revealing higher improvements in nanocomposites added with treated HNT.

Keywords

Halloysite nanotubes; Linear low density polyethylene (LLDPE); Nanocomposite; Thermal properties; Mechanical properties; Fracture toughness.

1. Introduction

Reinforcing thermoplastic polymers with nanotubes or nanoplatelets to form nanocomposites is a way to increase the usage of polymeric materials in engineering applications by improving their mechanical properties, namely elastic modulus and yield stress with filler contents as low as 5–10 wt% [1-3]. Furthermore, filler's shape, dimension, aspect ratio and surface characteristics play a key role in determining the morphology and thus the thermo-mechanical, rheological, flame resistance and optical properties of the final composite [4, 5]. In particular, nanofillers such as carbon nanotubes (CNTs) [6-9], nanoclay (especially montmorillonite (MMT)) [10-13] and graphite nanoplatelets [14-16] have attracted great attention in the past decades for the production of nanocomposites based on engineered polymers such as polypropylene (PP), polyethylenes (PEs), polyamide (PA), rubbers and epoxy resins [17-26].

Nonetheless, most of the reported literature indicate that there is a significant reduction in the elongation at break and/or impact strength in these materials when the nanofiller is added and when its content increases [18, 27]. Consequently, the use of nanocomposites may be limited by the losses in toughness. On the other hand, nanofillers such as halloysite nanotubes (HNTs) makes it possible, contrary to other nanofillers, to significantly reduce the ductility loss upon addition in a ductile matrix (PP [28] or PA6 [21] for example). Moreover the addition of HNT, event at high content, has a moderate effect on the flow behavior of the polymer which can still be processed as the neat material [29, 30]. Halloysite is a kind of clay aluminosilicate mineral with hollow nanotubular structure mined from natural deposits. Chemically similar to kaolin, halloysite has a molecular formula of $\text{Al}_2\text{Si}_2\text{O}_5(\text{OH})_4 \cdot n\text{H}_2\text{O}$ with 1:1 layer. Nanotubular geometry of halloysites exhibits nanoscale dimensions, with a typical length in the range of 0.1 - 15 μm , inner diameter of 5 - 30 nm and outer diameter of 30 - 70 nm, depending on the deposits [31]. Various features of halloysite nanotubes (HNTs) like rigidity, high aspect ratio and low density of surface hydroxyl groups compared with other silicates make it a promising reinforcing filler for polymer materials. Furthermore, its abundant availability, biocompatibility and low price promoted HNTs as subject of recent research. When compared with carbon nanotubes (CNTs), the naturally occurring HNTs are much cheaper and easily available. In particular, HNTs have high mechanical strength and modulus and these features make it an ideal material for the fabrication of high-performance polymer nanocomposites [32]. Recently, HNTs are being attempted to utilize as nanofiller in conjunction with various polymers such as PP, PA, rubber

and epoxy resin generally for strengthening and toughening of the matrix, but also to improve their thermal stability and flame retardancy and to reduce the coefficient of thermal expansion [32-34]. On the other hand, many approaches and techniques have been utilized to realize nanocomposites with unique structures and desired performance [35].

It is expected that HNTs could be dispersed relatively uniformly in thermoplastics by direct melt blending, especially for polymers with high polarity such as PAs. Nevertheless, compatibilization between polyolefins and inorganics is challenging due to the great polarity discrepancy and the chemical inertness of the polyolefins. To increase the compatibility between PP and HNTs, Du et al. proposed a two-step method of grafting PP chains onto the surface of HNTs [36].

Modifications at the surfaces of HNTs provide an opportunity to expand the basal spacing of HNTs through intercalation of inorganic and organic compounds in their internal layers. This contributes to a better and more homogeneous dispersion of HNTs within the corresponding polymer during melt blending. Furthermore, the surface modification can remarkably enhance the wettability of the filler and adhesion between filler and matrix [37].

Thermoplastic/HNT nanocomposites exhibit markedly increased storage moduli and flexural strength. The positive effects of the HNTs on the performance of the polymeric matrix are correlated with the unique characteristics of the HNTs, the uniform dispersion and the possible interfacial reactions between the modified HNTs and the matrix. The existing literature suggests that these nanocomposites possess excellent performance including reinforcing effects, enhanced flame retardancy and reduced thermal expansion.

HNTs in various concentrations (5-30%) were used for preparing nanocomposites based on PA6 by simple melt extrusion process. It was found that HNTs influenced the fire performance of the composites, by developing thermal insulation barrier at their surface during burning.

Nevertheless, relatively high concentrations of additive (15 wt%) are required to achieve the adequate level of fire retardancy similar to nanoclay additives [38].

Linear low density polyethylene (LLDPE) is an important thermoplastic for the applications such as electric wire, cable, film, pipe and container [39]. However, its applications are limited, especially due to its relatively low strength, low softening point and flammability resistance. Therefore, it is necessary to modify LLDPE with the incorporation of nanofillers to get improved mechanical properties, flame retardancy as well thermal stability [40-43]. Furthermore, both thermal and mechanical properties can be further enhanced by the addition of graft copolymers

[44] which improve the dispersion degree of the filler and interface properties between filler and matrix.

The effects of HNTs on the flame retardancy of LLDPE were studied by Jia et al., with the results suggesting that HNTs are expected to be promising flame-retardant additives for LLDPE [44].

Moreover, Dorigato et al. studied the role of fumed silica nanoparticles, having different surface area and surface treatments, on the fracture behavior of LLDPE matrix through the essential work of fracture method (EWF). The cited authors found prominent increments in both the initiation and the propagation terms of the specific work of fracture [45].

Researchers have recently focused on the study of the fracture toughness of a wide range of polymeric nanocomposites adopting the EWF method [46, 47], because of its simple specimens' preparation, easy testing and simple data reduction procedure [48]. In one of our previous work, we attempted to investigate the fracture toughness of LLDPE-boehmite alumina (BA) nanocomposites through EWF method, observing a toughness enhancement effect due to the nanofiller incorporation, but no particular dependence on the BA crystallite size and surface functionalization [49]. To the best of our knowledge, only few papers addressed the study of the effect of HNTs loading on the toughening mechanism of thermoplastic nanocomposites through the EWF method [21].

The present work aims at highlighting the enhancing effect of HNTs addition on the thermo-mechanical and rheological properties of LLDPE. Particular emphasis has been devoted to assess the fracture behavior evaluated by the EWF approach.

2. Experimental section

2.1 Materials and samples preparation

The matrix used in this work was a Flexirene[®] CL10 linear low-density polyethylene (MFI at 190 °C and 2.16 kg = 2.6 g/10', Mn = 27000 g·mol⁻¹, density = 0.918 g·cm⁻³), produced by Polimeri Europa S.p.A. (Mantova, Italy) using Ziegler-Natta catalysis and butene as a comonomer (C₄-LLDPE). This type of linear low density polyethylene, additivated with antioxidants, is suitable for cast extrusion of thin film with high optical properties.

Untreated HNT, denoted as uHNT, were mined from ?? (Turkey) and presented an oxide composition as follows (wt/wt%): SiO₂ (46.7%), Al₂O₃ (33.1%), Fe₂O₃ (2.96%), CaO (0.37%), MgO (0.26%), Na₂O (0.12%), K₂O (0.27%), TiO₂ (0.03%). Treated HNT (tHNT) were mined from Szegilon (Hungary) and presented a different morphology and surface properties due to a chemical treatment of the initial kaolinite. The preparation of tHNT can be described as follow: intercalation with K-acetate (CH₃CO₂K) (30:70 wt% K-acetate/wt% kaolinite), drying (T=110 °C, t=24 h), treatment with ethylene glycol (C₂H₆O₂) (5:1 mol ethylene glycol/mol kaolinite, T=150 °C, t=4 h) and final treatment with hexamethylenetetramine ((CH₂)₆N₄) (5:1 mol Hexamethylenetetramine/mol kaolinite, T=20 °C, t=48 h). After each step the degree of intercalation was determined by X-ray diffraction (XRD). Generally, complete delamination was achieved when the last step (treatment with hexamethylenetetramine) was repeated one more time. The excess reagents were removed from the particles' surface after each step with washing with acetone (using a G4-type filter). After the last step, excess reagent was removed by drying at 50 °C for 2 hours.

Table 1 summarizes the experimental density, Brunauer-Emmett-Teller (BET) specific surface area and the diffraction pattern characteristics of the HNTs used in this work.

LLDPE was used as received while the fillers were dried at 80 °C for 12 h prior to use. The samples were prepared by melt compounding in a Brabender[®] Plasti-Corder internal mixer (T=170 °C, n=50 rpm, t=15 min) followed by compression moulding using a Collin[®] P200E hot press (T=170 °C, p=2 MPa, t=15 min), in order to get plane sheets with thickness of around 0.5 mm. The filler content was varied between 0 and 8 wt%.

The unfilled matrix was denoted as LLDPE, while nanocomposites were designated indicating the matrix, the filler type and the filler weight amount. For instance, a sample filled with 4 wt% of untreated HNT is indicated as LLDPE-uHNT-4.

2.2 Experimental techniques

2.2.1 Filler characterization

Density measurements were carried out through helium pycnometry technique (Micromeritics[®] Accupyc 1330 helium pycnometer, Norcross USA), at a temperature of 23 °C, using a testing chamber of 3.5 cm³.

XRD analyses were performed through a Rigaku[®] 3D Max X-Ray diffractometer, scanning the samples in a 2θ range between 3° and 67°, at a 2θ step of 0.1°. The wavelength of the X-Ray source was 0.15418 nm.

In order to evaluate the morphological features of HNTs, transmission electron microscope (TEM) micrographs were taken through a Philips[®] CM12 transmission electron microscope adopting an acceleration voltage of 120 keV. The powder samples used for the observations were dispersed in a solution of acetone and sonicated for 5 minutes prior to observations.

2.2.2 Nanocomposite characterization

2.2.2.1 Spectroscopy analyses

The dispersion state of the HNT particles in the LLDPE was studied by scanning electron microscopy (SEM) using a FEI Quanta 250 FEG device (FEI, Hillsboro, Oregon, USA).

Specimens were cryomicrotomed with a Diatome diamond knife at $T = -120^\circ\text{C}$ using a Leica EM UC6 ultramicrotome equipped with a cryo-chamber. The cryocut surfaces of the specimens were inspected in SEM (acceleration voltage 10 kV) without sputtering, using a high resolution vCD detector for backscattered electrons. The morphology of the samples was also studied in a transmission electron microscope (TEM). The TEM device (Zeiss LEO 912 Omega, Oberkochen, Germany) was working at an acceleration voltage of 120 kV. Thin specimens (ca. 50 nm), prepared by cryocutting with the above ultramicrotome at $T = -120^\circ\text{C}$, were subjected to TEM investigations without any staining.

XRD analysis were performed through a Rigaku® 3D Max X-Ray diffractometer, scanning the samples in a 2θ range between 3° and 67° , at a 2θ step of 0.1° . The wavelength of the X-Ray source was 0.15418 nm.

IR spectroscopic study was carried out on 80 μm thick nanocomposite films within a scanning interval between 650 and 4000 cm^{-1} , setting a resolution of 2 cm^{-1} for a total number of co-added scans of 64. Utilizing the same operative parameters, IR spectra were taken on the nanofillers alone, too.

2.2.2.2 Rheology measurements

The melt rheology of the nanocomposites was analyzed by an Rheoplus 32 V3 dynamic oscillatory rheometer (Anton Paar Physics, Ostfildern, Germany) working under controlled strain conditions. The test geometry was cone-plate (cone angle= 1°) with a cone diameter of 25 mm. Compression molded disks of around 0.6 mm thickness were placed between the plates hold at $T = 180^\circ\text{C}$. The thickness of the gap was set for 0.5 mm by squeezing the initial LLDPE disk. Frequency sweep tests were carried out at $T=180^\circ\text{C}$. During the measurement a small amplitude (1%) oscillatory shear was applied to the samples. The storage and loss shear moduli (G' and G'' , respectively) and the dynamic viscosity $|\eta^*|$ were measured as a function of angular frequency (ω) in the range 0.01–100 rad/s.

2.2.2.3 Thermal analyses

Differential scanning calorimetry (DSC) tests were carried out by a Mettler® DSC30 apparatus (Schwerzenbach, Switzerland) under a constant nitrogen flow of $100\text{ ml}\cdot\text{min}^{-1}$. The samples were heated up to 200°C at a rate of $10^\circ\text{C}\cdot\text{min}^{-1}$ with subsequent crystallization test down to 0°C , setting a cooling rate of $10^\circ\text{C}\cdot\text{min}^{-1}$. A subsequent heating scan was performed at $10^\circ\text{C}\cdot\text{min}^{-1}$. The melting enthalpy of 100% crystalline polyethylene has been considered as $\Delta H^0 = 290\text{ J}\cdot\text{g}^{-1}$ [50]. Moreover, the crystallinity χ_c of nanocomposite samples was calculated by taking the weight fraction of LLDPE in the composite into account. The melting temperatures T_{m1} and T_{m2} were recorded during the first and second heating scan, respectively. The crystallization enthalpy ΔH_c was measured by integrating the heat flow curve registered during cooling.

Thermogravimetric analyses (TGA) were carried out through a Q5000 IR thermogravimetric analyzer (TA Instruments-Waters LLC, New Castle, USA) imposing a temperature ramp between 40 and 700 °C at a heating rate of 10 °C·min⁻¹ under a constant nitrogen flow of 25 ml·min⁻¹. The onset of degradation temperature ($T_{d,onset}$) was determined by the point of intersection of tangents to two branches of the thermogravimetric curve, while the maximum rate of degradation temperature ($T_{d,max}$) was determined from the peak maxima in the first derivative of weight loss curve. Furthermore, the maximum mass loss rate (MMLR) was also recorded at $T_{d,max}$.

2.2.2.4 Mechanical tests

Uniaxial tensile tests were performed with an Instron[®] 4502 (Norwood, USA) tensile machine on samples of at least five ISO 527 type 1BA specimens. The tests were carried out at a crosshead speed of 0.25 mm·min⁻¹ up to a maximum axial deformation of 1%. The strain was recorded by using a resistance extensometer Instron[®] model 2620-601 with a gage length of 12.5 mm. The elastic modulus was measured as secant modulus between deformation levels of 0.05 % and 0.25 % in according to ISO 527 standard. Uniaxial tensile properties, such as stress at yield (σ_y), stress at break (σ_b) and strain at break (ϵ_b) were determined at a higher crosshead speed (50 mm·min⁻¹) without extensometer.

Creep tests were performed utilizing a dynamic mechanical analyzer DMA Q800 (TA Instruments[®]-Waters LLC, New Castle, USA) applying a constant stress (σ_0) of 1 MPa (i.e 10% of the stress at yield of unfilled LLDPE) for 3600 s at 30 °C. Rectangular specimens, 25 mm long, 5 mm wide and 0.5 mm thick, were used whereby setting a gage length of 11.5 mm. The creep compliance $D(t)$, computed as the ratio between the strain and the creep stress, was plotted against the time for the different samples.

Dynamic mechanical analyses (DMA) were carried out at a DMA Q800 testing machine (TA Instruments[®]-Waters LLC, New Castle, USA) on film specimens 25 mm long, 5 mm wide and 0.5 mm thick. The samples were analyzed over a temperature range between -130 °C and 80 °C, imposing a heating rate of 3 °C·min⁻¹ and a frequency of 1 Hz. A preload of 0.2 MPa and a maximum strain of 0.05 % were set for each test. The most important viscoelastic parameters (E' , E'' , $\tan(\delta)$) were recorded at different temperatures.

The toughening mechanism associated to the presence of HNT nanotubes in LLDPE was assessed through the Essential Work of Fracture (EWF) method under tensile conditions.

According to the methodology proposed by Williams et al. [51], the total fracture energy (W_f) spent to bring a pre-cracked body to complete failure can be partitioned into an essential work (W_e) done in the fracture zone to create new surfaces that is intrinsic to the fracture of the material and a non-essential work (W_p) done in the outer plastic zone related to plastic work dissipation in the process zone. In plane stress conditions, the essential work of fracture should be proportional to the ligament length of the sample (L), whereas the non-essential work of should be proportional to L^2

$$W_f = W_e + W_p = w_f L B = w_e L B + w_p \beta L^2 B \quad (1)$$

which can be written in the specific terms as

$$w_f = w_e + \beta w_p L \quad (2)$$

where B is the specimen thickness, β is a shape factor depending on both the material and the geometry of the body, w_e is the specific essential work of fracture, w_p is the specific non-essential work of fracture. The quantities w_e and βw_p are determined by a linear interpolation of a series of experimental data of w_f obtained by testing specimens having different ligament lengths. The quantity w_p can be explicitly deduced for some shapes of the outer plastic zone with known β e.g., for circular, elliptical and diamond-type zones β is given by $\pi/4$, $\pi h/4L$, and $h/2L$, respectively, where h is the height of the corresponding zone [48].

Furthermore, the specific total work of fracture (w_f) can be divided into specific work of fracture for yielding (w_y) and specific work of necking (w_n) ([48] and references therein):

$$w_f = w_y + w_n = (w_{e,y} + \beta' w_{p,y} L) + (w_{e,n} + \beta'' w_{p,n} L) \quad (3)$$

DENT specimens (width 30 mm, height 80 mm, thickness 0.5 mm, distance between the grips 50 mm) were tested with an Instron[®] 4502 (Norwood, USA) tensile machine. At least four tests were conducted for every ligament length, and five different ligament lengths between 5 and 13 mm were tested setting a crosshead speed of 10 mm·min⁻¹. The notches were introduced by using a home made apparatus mounting a razor blade, in order to obtain a very sharp crack tip. From

SEM images it was possible to estimate an average crack tip radius of less than 20 μm . The exact ligament lengths were measured with a profile projector with an accuracy of 0.01 mm.

In order to study the fracture behavior of the material at high strain rate levels, tensile impact tests were carried out with a CEAST[®] (Norwood, USA) tensile impact instrumented pendulum.

The striker, with a mass of 3.65 kg and an initial angular position of 63°, had an impact speed of 2 $\text{m}\cdot\text{s}^{-1}$ and a total impact energy of 7.3 J. The specific tensile energy to break (TEB), obtained by integrating load-displacement curves, was obtained by applying Eq (4).

$$TEB = \frac{1}{A} \left[V_0 \int_0^{tr} F dt - \frac{1}{2m} \left[\int_0^{tr} F dt \right]^2 \right] \quad (4)$$

where A is the cross section of the specimen, m is the striker mass and V_0 is the impact speed.

3. Results and discussion

The morphological characteristics of uHNT and tHNT were obtained from TEM micrographs depicted in [Figure 1a](#) and [Figure 1b](#), respectively. Firstly, it is worth mentioning that HNT mined from different sources can vary in the level of hydration, morphology (dimension of inner and outer diameter, length and aspect ratio) and colour, depending on the substitutional metals and on mineral origin [37]. uHNT was present in a high proportion of thick unexfoliated stacks, few platy particles and very short tubes. On the other hand, the effect of the exfoliation promoted by chemical treatment is observable in the case of tHNT, mainly represented by platy particles and more and longer tubular elements, with an electron-transparent central lumen.

In particular, the tubular particles showed dimensions within the ranges of outer diameter 30-60 nm, inner diameter 6-20 nm and length 150 nm - 2 μm . The thickness of the HNT wall is around 5-25 nm.

The data of density measured through helium pycnometry on the two HNT are reported in [Table 1](#). In particular, tHNT presents a density 23% lower with respect to uHNT, clearly indicating an higher degree of exfoliation and dispersion of the tHNT particles due to chemical treatment, as confirmed by TEM observations.

3.1 Morphology

In order to investigate the effect of the HNTs treatment on the morphology and on the interface properties between filler and LLDPE, cryocut surfaces of composites were examined through SEM analysis. In particular, SEM pictures taken from the cryocut surfaces of LLDPE composites with 4 wt% and 8 wt% tHNT are represented in [Figure 2a-b](#). It is evident from the SEM microphotographs of LLDPE-tHNT that the nanotubes are finely and homogeneously dispersed within the matrix even at 8 wt % filler loading. The observations of good dispersion are consistent with the mechanical performance improvement reported later. The poor dispersion of uHNT in form of numerous and big agglomerates are clearly observable also by naked eye. For the latter reason, the authors decided not to show SEM and TEM micrographs of LLDPE-uHNT composites.

TEM pictures confirm that the designation nanocomposite is correctly used ([Figure 3a-b](#)) in the case of LLDPE-tHNT composites. Both SEM and TEM morphological analysis confirm that tHNT can be finely dispersed within the LLDPE matrix even at high filler contents and without using polymeric compatibilizer, while uHNT tends to form micrometric aggregates and agglomerates producing negative effects on the mechanical properties.

XRD diffractograms of the tHNT and uHNT are displayed in [Figure 4a](#). The most relevant values of 2θ and their relative basal spacing are also presented in [Table 1](#). In particular, tHNT and uHNT show a small reflection at $2\theta_{001,t} = 12.41^\circ$ and $2\theta_{001,u} = 13.26^\circ$, respectively, which is related to the the 001 crystallographic plane. The correspondent basal spacing is equal to 0.713 nm and 0.667 nm, respectively, confirming the multiwall nanotubular structures at nanoscale of HNT. Furthermore, the difference found in the basal spacings suggests that exfoliation occurred in tHNT owing to the chemical treatment used.

Other relevant reflections are located at higher values of 2θ , corresponding to the 020 and 002 crystallographic planes. Interestingly, no significant difference can be noticed between the XRD spectra of tHNT and uHNT.

According to XRD diffractograms of LLDPE nanocomposites, the intensity of the signals of all HNT characteristic peaks slightly increases with the nanofiller amount and becomes well recognizable in the diffractograms of composites with 8 wt% HNT ([Figure 4b](#)). These peaks can confirm the presence of structures with limited intercalation and can be attributed to the formation of nanocomposites. Nevertheless, both reflections of HNT at around $2\theta=20.4^\circ$ and

$2\theta=24.7^\circ$ are overlapped by characteristic LLDPE reflections and it results difficult to estimate an amplitude increase dependent on the nanofiller type and amount.

Representative IR spectra of the unfilled LLDPE and corresponding nanocomposites with tHNT and uHNT are plotted for comparison in [Figure 5a](#) and [Figure 5b](#), respectively. Furthermore, the IR spectra of the HNT nanopowders are included in the correspondent plots. Most of the peaks recognizable in the IR spectrum of tHNT nanopowder correspond to those reported in the literature [33, 52, 53]. In particular, the bands at 797 and 755 cm^{-1} are assigned to translational vibrations of the external OH groups as well as out-of-plane OH bending, while the peak at 695 cm^{-1} is related to the perpendicular Si-O stretching bond. The absorption bands nearby 1092 and 1030 cm^{-1} are assigned to stretching vibration of Si-O bonds, while the characteristic absorption band at 912 cm^{-1} is due to flexural vibrations of Al-OH. The results confirm coexistence of hydroxyl groups and Si-O bonds on the surfaces of HNTs.

The peak at 1327 cm^{-1} is associated to CH_3 deformation. The absorption peaks at 1558 and 1467 cm^{-1} are assigned to C = O antisymmetric and symmetric stretching vibrations, respectively, while the peaks located at 2956, 2926 and 2857 cm^{-1} are attributed to C-H stretch vibrations [54]. The absorption band at 3622 cm^{-1} is the characteristic absorption of hydroxyl groups located on shared interfaces of layered structure consisting of silicon-oxygen tetrahedron and aluminium-oxygen octahedron, and the band at 3694 cm^{-1} is the characteristic absorption of external hydroxyl groups located on non-shared surfaces of the layered structure [44].

On the other hand, when considering the IR spectrum of uHNT, it is noticeable that the characteristic peaks attributable to the K-acetate and hexamethylenetetramine located within the bands 1327-1558 cm^{-1} and 2857-2956 cm^{-1} are absent, while the typical peaks of HNT are mostly reduced or suppressed. In particular, limited peaks are observable at 3622 and 3694 cm^{-1} , indicating a lower density of inner surface hydroxyl groups. Moreover, the bands at 695, 755 and 797 cm^{-1} are also suppressed and thus appear as traces.

The spectra of LLDPE-tHNT nanocomposites present the characteristic peaks attributable to tHNT, whose intensity increases with the filler content. On the other hand, no significant difference can be observed among the spectra of LLDPE-uHNT samples, clearly indicating a lower degree of chemical interaction between filler and matrix by contrast to the LLDPE-tHNT composites.

3.2 Rheological behavior

The effect of the filler addition on the isothermal frequency dependence of the dynamic shear storage modulus (G') and complex viscosity ($|\eta^*|$) is reported in [Figure 6a](#) for unfilled LLDPE and LLDPE composites filled with 4 wt% HNT. A general decrease in both G' and $|\eta^*|$ can be easily detected for all LLDPE-HNT-4 nanocomposites over the whole frequency range. A similar decrease of both G' and $|\eta^*|$ is also recorded in the case of composites filled with 8 wt% HNT ([Figure 6b](#)). For both LLDPE-HNT-4 and LLDPE-HNT-8 practically no difference is observable as a function of the HNT types. Noteworthy, the lowering in viscosity is very beneficial for the material processing. Moreover, some deviations in the measured parameters can be observed at low frequencies, mainly with respect to the G' values. This experimental error is most likely due to the cone-plate configuration used.

Incorporation of nanofillers in thermoplastics is generally associated with a marked increase in the melt viscosity, at least in the range of low frequencies. Furthermore, a prominent enhancement in G' is usually observed. These changes are normally assigned to a pseudo solid-like transition caused by the dispersed nanoparticles [55-61]. Nevertheless, the lowering of both $|\eta^*|$ and G' by HNT addition to LLDPE is opposed to that general trend. Khumalo et al. observed a similar rheological behaviour in the case of PE filled with synthetic boehmite alumina (BA) nanocomposites [62]. In one of our previous work, we studied the rheological behaviour of LLDPE nanocomposites added with BA and found that the addition of the filler produces a decrease in $|\eta^*|$ and G' compared to unfilled LLDPE [49].

Fernandez et al. studied PA6 nanocomposites with HNT, observing a markedly lower viscosity in the molten nanocomposites up to a filler content as high as 30 wt% [30].

The viscosity decrease recorded in LLDPE nanocomposites might be ascribed to the morphology of the polymer chains. In fact, LLDPE is a highly branched polymer whose chains would tend to get entangled and apparently HNT particles can fill in the spaces between chain branches. This provides some “rigidity” enabling easier flow [29]. Nevertheless, future research is required in order to give further clarifications on the mechanisms of decrease in viscosity in polyolefins by HNT incorporation.

3.3 Thermal properties

The addition of the filler produces a moderate increase of the crystallization temperature in both uHNT and tHNT nanocomposites, but no particular dependence of nucleating effect on the HNT type is evidenced (Table 2). Furthermore, the crystallization temperature seems to approach a plateau for HNT content as high as 4 wt%.

The nucleating effect of HNT was already reported in previous papers regarding PA6 [35] and PP nanocomposites [63]. Interestingly, Liu et al. investigated isotactic PP added with HNT and found HNT to have dual nucleating ability for α and β crystalline forms of PP under appropriate kinetics conditions [63]. It was also claimed that the formation of the β crystalline form in the PP composites is correlated to the unique surface characteristics of the HNT. Recently, Guo et al. studied the non-isothermal crystallization behavior and the polymorphism of PA6 and PA6/HNT nanocomposites [19]. It was found that HNT acts as nucleating agent, accelerates the crystallization and induces the formation of γ -phase crystals. These results suggest that, similar to other nanosized inorganic fillers, such as silica and MMT, HNTs serve as nucleation agents and facilitate the crystallization of the nanocomposites [35].

Concurrently, the melting temperature recorded during the second scan (T_{m2}) and the crystallinity (χ_c) are slightly higher in LLDPE nanocomposites, but do not seem to have a direct correlation with the nanofiller content.

The thermal resistance parameters as detected in TGA measurements are reported in Table 3. When considering LLDPE-HNT nanocomposites, both $T_{d,onset}$ and $T_{d,max}$ markedly increase with the filler content, showing a slightly higher efficiency in LLDPE-tHNT samples. Improved thermal stability due to the addition of HNT has been already reported for PA6 [38] and PP [64] nanocomposites. Apart from acting as thermal stability agent, HNTs have also been demonstrated as effective flame-retardant agents for PP, LLDPE and PA6, probably thanks to the hollow tubular structures of HNT which constitutes a barrier for heat and mass transport and the presence of iron oxide and other oxides in the HNTs [35].

Interestingly, the char content recorded for LLDPE nanocomposites is markedly lower than the added amount of filler, indicating that the filler encountered a prominent weight loss during heating. This is probably due to release of crystal water in the range between 430 and 570 °C [44]. In particular, the lower char content observed in tHNT with respect to uHNT can be attributed to the two causes: the degradation and further loss of the functional groups derived

from the chemical treatment of tHNT and the possible higher content of crystal water tHNT.

Recall, that tHNT and uHNT were mined from different zones.

During the thermal degradation of the specimen, filler aggregates usually tend to agglomerate on the surface of the molten polymer, thus creating a barrier that physically protects the rest of the polymer and hinders the volatilization of the oligomers generated during the combustion process [65]. Thus, in general the higher the filler amount the lower the maximum mass loss rate (MMLR). However, this is not the case, as an higher content of HNT is associated to a greater MMLR (Table 3). In fact, the filler weight loss increases with the HNT content and this effect is probably preponderant on the MMLR decrease due to creation of physical barrier by filler aggregates.

3.4 Mechanical properties

As reported in Table 4a, the addition of HNT nanoparticles produces a significant increase of the elastic modulus of the LLDPE matrix, showing an higher efficiency in the case of tHNT. In particular, an improvement of 94% is reached for systems filled with 8 wt% of tHNT, compared to unfilled LLDPE.

The reinforcing effect provided by nanofiller incorporation is most often explained by the formation of an interphase region between the matrix and the particles. It has also been demonstrated that nanoparticles agglomeration is another significant mechanism responsible for stiffness increases in polymer nanocomposites [66]. A new approach, developed by Dorigato et al., was adopted in order to model the elastic properties of LLDPE-HNT nanocomposites taking into account the stiffening effect provided by nanoparticles composed of primary aggregates and agglomerates. Note that the hypothesis behind this model is that part of the polymer matrix is mechanically constrained within the aggregates and agglomerates [41, 49]. In order to implement the model, the Poisson's ratio of matrix and filler were chosen as 0.44 and 0.22, respectively, while the elastic modulus of filler was set to 300 GPa in according to literature data [67, 68].

The relative elastic modulus of the LLDPE-HNT composites is plotted in Figure 7 as a function of the filler volume fraction, along with the fitting curves obtained with the adopted model. It can be noticed that the proposed model can predict quite well the elastic modulus of LLDPE-tHNT-x and LLDPE-uHNT-x composites over the whole range of filler concentration. Furthermore, the significant increase of the elastic modulus detected for nanocomposites is associated to elevated

α values, which indicates the fraction of matrix constrained by nanoparticles. As already noticed by Dorigato et al. when applying the model in the case of LLDPE filled with fumed silica nanoparticles, there exists an apparent correlation between the α parameter and filler surface area [66] (Table 1). Specifically, tHNT possesses greater surface area than uHNT due to higher exfoliation, indicating higher capability of being intercalated by polymer matrix during compounding, with a consequent greater fraction of matrix constrained by nanoparticles' agglomerates.

The yield stress and stress at break decrease with the filler content in the case of LLDPE-uHNT nanocomposites, probably because of extensive filler aggregation [27]. For the same reason the elongation at break is lower than that of unfilled LLDPE. The increasing brittleness of the composites with filler content was also revealed by the tensile energy at break recorded during quasi-static tensile tests (TEB_{qs}). In particular, the presence of HNT particles causes stress concentration at the filler surface. Furthermore, interfacial failure might be more pronounced with increasing loading of halloysite.

On the other hand, the yield stress appears slightly higher in LLDPE-tHNT composites with respect to LLDPE, while stress at break and elongation at break moderately decrease, showing a stiffening effect which only slightly reduces the matrix ductility up to a filler content of 8 wt%. Similar behavior at yield and at break was found by Hadge in PA6-HNT nanocomposites [69] and Prashantha in PP-HNT samples [21].

In Figure 8 the isothermal creep compliance of unfilled LLDPE and composites added with 4 and 8 wt% HNT, under a constant load of 1 MPa and at 30 °C, is reported, while in Table 5 the elastic (D_e) and total components of the creep compliance after 2000 s ($D_{tot,2000}$) are summarized. The introduction of HNTs leads to a significant improvement of the creep stability of the material. It is generally believed that nanoparticles can effectively restrict the motion of polymer chains, influencing the stress transfer at nanoscale, with positive effects on the creep resistance of the material [70]. Furthermore, the addition of tHNT results in the best creep resistance, probably due to the better restriction of molecular chains during the viscous flow, showing a dependence on the HNT surface area and exfoliation.

The storage modulus (E') increases markedly with increasing HNT content, probably due to the restrictions of the molecular chains motion (Table 5), indicating that the incorporation of HNT nanoparticles remarkably enhances stiffness and load bearing capability of the material. As

already seen in the case of tensile properties and creep resistance, the addition of tHNT produces the highest improvement in E' . The enhancement of the thermo-mechanical properties can be attributed to three factors: the high intrinsic stiffness of the nanotubes resulting from their tubular structure, the interaction between filler and matrix and their good dispersion within the matrix [20]. However, only the first two factors seem to be responsible for the increased modulus in LLDPE-uHNT nanocomposites, while the third factor may be at work in the case of LLDPE-tHNT, which is in line with SEM observations.

On the other hand, the loss modulus (E'') increases remarkably with increasing HNT content, without a clear dependence on the HNT type. The glass transition temperature (T_g), as extrapolated from the $\tan \delta$ peak, was slightly higher for all nanocomposites with respect to unfilled LLDPE. In particular, the addition of HNTs into the LLDPE matrix may have two opposing effects on the T_g of the polymer: (i) a T_g decrease associated to the reduced entanglements and interactions among LLDPE chains due to the presence of the nanotubes whereby enhancing the motion of the polymer chains, and (ii) a T_g increase caused by a restriction of the segmental motion of LLDPE chains located near the nanotubes' surface in the interphase [20].

In the LLDPE-uHNT nanocomposites, the HNTs might reduce the intermolecular interactions among LLDPE chains and thus the T_g reduction dominates. However, above 4 wt% HNTs, this effect is compensated by the interactions between HNTs and LLDPE chains. Therefore, T_g shifts to slightly higher temperatures. On the other hand, in LLDPE-tHNT nanocomposites the restriction of the polymer chains' mobility dominates. This is probably due to the better dispersion of tHNT nanotubes, resulting in higher T_g . Comparison plots of the storage modulus (E') and loss factor ($\tan \delta$) are depicted in [Figure 9](#), as a function of temperature, for LLDPE and related nanocomposites.

The EWF method was applied to characterize the fracture behavior. At first, the basic preconditions necessary for the application of the EWF methodology were verified [51]. In particular, the validity criterion verifies that all tests were conducted under plane-stress state. Furthermore, all the specimens exhibited delayed yielding (i.e. ligament yielding is time-dependent and finishes when the crack has already started propagating), with subsequent ductile fracture, showing a large plastic deformation zone surrounding crack tip. Moreover, most specimens manifested evident necking after yielding, in agreement with Eq. (4). Since the force -

displacement curves of specimens with different ligament lengths were geometrically similar, the fracture mechanism was probably independent on the ligament length.

In particular, in all LLDPE-tHNT nanocomposites, the area under the curve after the maximum force was reached is higher than that prior to maximum force, indicating slow crack propagation with high energy absorption, typical of ductile materials [48] (Figure 10A). This is a clear indication that the addition of tHNT improves the strength of LLDPE without embrittlement of the material.

The elliptical shape of the stress-whitened zone (characterized by the shape factor β) formed during tensile EWF test performed on LLDPE nanocomposites was similar to that of neat LLDPE with slight variation in the height of the zone. The total specific EWF, the specific EWF at yielding and the specific EWF for necking were obtained by linear fits and tabulated in Table 6. A significant improvement in w_e is noticed with increase in tHNT content, whereas $\beta \square w_p$ values slightly decrease upon filler addition. These results indicate that tHNT addition significantly toughened the matrix [48].

Moreover, partitioned components of total EWF, such as EWF for yielding ($w_{e,y}$) and EWF for necking ($w_{e,n}$), also show an improvement in all nanocomposites when compared to unfilled LLDPE. In particular, the improvement in $w_{e,y}$ is probably due to the higher yield stress recorded for nanocomposites with respect to LLDPE, while the change in $w_{e,n}$ might be because of changes in the crack propagation behaviour in the nanocomposites [71].

On the other hand, LLDPE-uHNT composites show higher w_e only at 1 and 4 wt% concentrations, while the sample LLDPE-uHNT-8 manifests lower toughness properties, showing smaller w_e than unfilled LLDPE. Furthermore, the component $w_{e,y}$ is very high, while $w_{e,n}$ appears quite low compared to other nanocomposites. This indicates that most of the deformation energy is spent for yielding, while very low energy contributes to necking.

Moreover, the β factor appears lower than that of the other LLDPE-uHNT samples, indicating a clear reduction in the height of the deformation zone. Although the related specimens exhibit delayed yielding, the plastic deformation zone, formed by crazing, is highly constrained. The latter yields restricted necking during the subsequent deformation (Figure 10B). This behavior clearly indicates that the addition of uHNT at 8 wt% is associated with reinforcing effect and parallel to that with a prominent loss in ductility. This feature is in accordance with the results of the quasi-static tensile tests.

When the load is applied at high speed in tensile impact tests, the introduction of tHNT nanoparticles leads to an increase of the energy adsorbed at break (TEB) (Table 4b). This is in line with the TEB_{qs} data reported in quasi-static tensile tests (Table 4a). On the other hand, the addition of uHNT produces a slight decrease in TEB, proportional with the filler content. This is most likely due to extensive filler agglomeration and poor matrix/filler interfacial interaction. The enhancement in impact strength, found for LLDPE-tHNT specimens, can be ascribed to the beneficial effects of the well dispersed tHNT nanotubes. The latter are obviously triggering failure events linked with HNT debonding, pull-out and breakage phenomena. [21, 37, 72, 73]. Moreover, the crystallization of the polymer with the addition of the filler may affect the toughness, as well (Table 2) [74]. The better dispersion tHNT (based on SEM and TEM investigations) and the surface treatment (leading to better interfacial interaction) are further factors, which may be responsible for the observed improvement found for LLDPE-tHNT compared to LLDPE-uHNT nanocomposites.

4. Conclusion

LLDPE based composites were prepared through melt compounding and hot pressing using both untreated and treated HNT up to filler contents of 8 wt% in order to assess the role of the filler exfoliation and surface treatment on the thermal, mechanical and rheological properties of the resulting composites.

The addition of treated nanoparticles resulted in a better dispersion of the filler within the matrix, as confirmed by SEM and TEM observations. HNT nanotubes acted as a weak nucleating agent, producing an increase of the crystallization peak temperature. The melt viscosity of nanocomposites decreased with nanofiller incorporation, showing an interesting feature of practical relevance.

The mechanical properties of all samples were characterized by tensile test, creep tests and dynamic mechanical thermal analyses. The results of tensile tests indicated that the nanoparticles can reinforce LLDPE at a low filler content, especially in the case of treated HNT, without loss in ductility. Creep tests showed that creep compliance was markedly reduced by nanofiller incorporation, while storage and loss moduli were enhanced in all nanocomposites.

The toughness of the LLDPE-tHNT, evaluated through EWF method, outperformed both the LLDPE matrix and the LLDPE-uHNT nanocomposites. Incorporation of uHNT in 8 wt%

reduced the toughness even below that of the matrix. This was ascribed to differences in the dispersion and surface treatment of the HNT nanoparticles.

Acknowledgments

The authors greatly acknowledge Prof. Ceccato R. for the kind assistance in XRD analyses and rheological measurements at the Ceramurgy Laboratory of the Industrial Engineering Department at the University of Trento. Other acknowledgements are particularly due to the technician Gloria Ischia, Ph.D. for the TEM observations carried out at the Electronic Microscopy Laboratory of the Industrial Engineering Department.

References

- [1] Hussain F. Review article: Polymer-matrix Nanocomposites, Processing, Manufacturing, and Application: An Overview. *Journal of Composite Materials*. 2006;40(17):1511-1575.
- [2] Fu S, Feng X, Lauke B, Mai Y. Effects of particle size, particle/matrix interface adhesion and particle loading on mechanical properties of particulate-polymer composites. *Composites Part B: Engineering*. 2008;39(6):933-961.
- [3] Njuguna J, Pielichowski K, Desai S. Nanofiller-reinforced polymer nanocomposites. *Polymers for Advanced Technologies*. 2008;19(8):947-959.
- [4] Jancar J. Review of the role of the interphase in the control of composite performance on micro- and nano-length scales. *Journal of Materials Science*. 2008;43(20):6747-6757.
- [5] Sutherland LS, Sheno RA, Lewis SM. Size and scale effects in composites: I. Literature review. *Composites Science and Technology*. 1999;59:209 - 220.
- [6] Ma P-C, Siddiqui NA, Marom G, Kim J-K. Dispersion and functionalization of carbon nanotubes for polymer-based nanocomposites: A review. *Composites Part A: Applied Science and Manufacturing*. 2010;41(10):1345-1367.
- [7] Bhattacharyya AR, Sreekumar TV, Liu T, Kumar S, Ericson LM, Hauge RH, et al. Crystallization and orientation studies in polypropylene/single wall carbon nanotube composite. *Polymer*. 2003;44(8):2373-2377.
- [8] Kim JY. The effect of carbon nanotube on the physical properties of poly(butylene terephthalate) nanocomposite by simple melt blending. *Journal of Applied Polymer Science*. 2009;112(5):2589-2600.
- [9] Lau K, Gu C, Hui D. A critical review on nanotube and nanotube/nanoclay related polymer composite materials. *Composites Part B: Engineering*. 2006;37(6):425-436.
- [10] Pham Hoai Nam PM, Masami Okamoto, Tadao Kotaka, Naoki Hasegawa , , Usuki A. A hierarchical structure and properties of intercalated polypropylene/clay nanocomposites *Polymer*. 2001.
- [11] Perrinsarazin F, Tonthat M, Bureau M, Denault J. Micro- and nano-structure in polypropylene/clay nanocomposites. *Polymer*. 2005;46(25):11624-11634.
- [12] Panwar A, Choudhary V, Sharma DK. Review: A review: polystyrene/clay nanocomposites. *Journal of Reinforced Plastics and Composites*. 2011;30(5):446-459.
- [13] Olewnik E, Garman K, Czerwiński W. Thermal properties of new composites based on nanoclay, polyethylene and polypropylene. *Journal of Thermal Analysis and Calorimetry*. 2010;101(1):323-329.
- [14] Fukushima H. Graphite nanoreinforcements in polymer nanocomposites. East Lansing, MI, USA: Michigan State University; 2003.
- [15] Kalaitzidou K, Fukushima H, Drzal LT. Multifunctional polypropylene composites produced by incorporation of exfoliated graphite nanoplatelets. *Carbon*. 2007;45(7):1446-1452.
- [16] Sengupta R, Bhattacharya M, Bandyopadhyay S, Bhowmick AK. A review on the mechanical and electrical properties of graphite and modified graphite reinforced polymer composites. *Progress in Polymer Science*. 2011;36(5):638-670.
- [17] Xiaohui Liu QW. PP/clay nanocomposites prepared by grafting-melt intercalation. *Polymer*. 2001.
- [18] Chun Lei Wu MQZ, Min Zhi Rong, Klaus Friedrich. Tensile performance improvement of low nanoparticles filled-polypropylene composites *Composites Science and Technology*. 2002.

- [19] Guo B, Zou Q, Lei Y, Du M, Liu M, Jia D. Crystallization behavior of polyamide 6/halloysite nanotubes nanocomposites. *Thermochimica Acta*. 2009;484(1-2):48-56.
- [20] Lecouvet B, Gutierrez JG, Sclavons M, Bailly C. Structure–property relationships in polyamide 12/halloysite nanotube nanocomposites. *Polymer Degradation and Stability*. 2011;96(2):226-235.
- [21] Prashantha K, Schmitt H, Lacrampe MF, Krawczak P. Mechanical behaviour and essential work of fracture of halloysite nanotubes filled polyamide 6 nanocomposites. *Composites Science and Technology*. 2011;71(16):1859-1866.
- [22] Abdel-Aal N, Ei-Tantawy F, Al-Hajry A, Bououdina M. Epoxy resin/plasticized carbon black composites. Part I. Electrical and thermal properties and their applications. *Polymer Composites*. 2008;29(5):511-517.
- [23] Choi YK, Sugimoto K, Song SM, Gotoh Y, Ohkoshi Y, Endo M. Mechanical and physical properties of epoxy composites reinforced by vapor grown carbon nanofibers. *Carbon*. 2005;43(10):2199-2208.
- [24] Dorigato A, A.Pegoretti, F.Bondioli, M.Messori. Improving epoxy adhesives with zirconia nanoparticles. *Composite Interfaces*. 2010.
- [25] Gauthier C, Chazeau L, Prasse T, Cavaille JY. Reinforcement effects of vapour grown carbon nanofibres as fillers in rubbery matrices. *Composites Science and Technology*. 2005;65(2):335-343.
- [26] Tarawneh MA, Ahmad, S.Hj. , Yahya, S.Y. , Rasid, R. Effect of ultrasonic treatment on the tensile and impact properties of thermoplastic natural rubber nanocomposites reinforced with carbon nanotubes. In: *Proceedings AC, editor. International Conference on Nanoscience and Nanotechnology, Nano-SciTech 2008;. Selangor 2009. p. 71-75.*
- [27] Bikiaris DN, Vassiliou A, Pavlidou E, Karayannidis GP. Compatibilisation effect of PP-g-MA copolymer on iPP/SiO₂ nanocomposites prepared by melt mixing. *European Polymer Journal*. 2005;41(9):1965-1978.
- [28] Prashantha K. Processing and characterization of halloysite nanotubes filled polypropylene nanocomposites based on a masterbatch route: effect of halloysites treatment on structural and mechanical properties. *Express Polymer Letters*. 2011;5(4):295-307.
- [29] Blaszczyk P, Brostow W, Datashvili T, Lobland HEH. Rheology of low-density polyethylene + Boehmite composites. *Polymer Composites*. 2010;31(11):1909-1913.
- [30] Fernández A, Muniesa M, González J. Characterisation and Processing of Reinforced PA 6 with Halloysite Nanotubes (HNT) for Injection Molding. *Journal of Mechanical Engineering*. 2013;59:1-10.
- [31] Guo B, Chen F, Lei Y, Liu X, Wan J, Jia D. Styrene-butadiene rubber/halloysite nanotubes nanocomposites modified by sorbic acid. *Applied Surface Science*. 2009;255(16):7329-7336.
- [32] Rawtani D, Agrawal YK. Multifarious applications of halloysite nanotubes: a review. *Review of Advanced Material Science*. 2012;30:282-295.
- [33] Pasbakhsh P, Ismail H, Ahmad Fauzi MN, Abu Bakar A. Halloysite nanotubes as a novel nanofiller for polymer nanocomposites. 21st Australian Clay Minerals Conference. Brisbane 2010.
- [34] Rawtani D, Agrawal YK. Halloysite as support matrices: a review. *Emerging Materials Research*. 2012;1(4):212-220.
- [35] Du M, Guo B, Jia D. Newly emerging applications of halloysite nanotubes: a review. *Polymer International*. 2010;59:574-582.

- [36] Du M, Guo B, Liu M, Jia D. Preparation and Characterization of Polypropylene Grafted Halloysite and Their Compatibility Effect to Polypropylene/Halloysite Composite. *Polymer Journal*. 2006;38(11):1198-1204.
- [37] Murariu M, Dechief A-L, Paint Y, Peeterbroeck S, Bonnaud L, Dubois P. Polylactide (PLA)—Halloysite Nanocomposites: Production, Morphology and Key-Properties. *Journal of Polymers and the Environment*. 2012;20(4):932-943.
- [38] Marney DCO, Russell LJ, Wu DY, Nguyen T, Cramm D, Rigopoulos N, et al. The suitability of halloysite nanotubes as a fire retardant for nylon 6. *Polymer Degradation and Stability*. 2008;93(10):1971-1978.
- [39] James E. *Polymer data handbook*. New York: Oxford University Press; 1999.
- [40] Dorigato A. Linear low-density polyethylene/silica micro- and nanocomposites: dynamic rheological measurements and modelling. *eXPRESS Polymer Letters*. 2010;4(2):115-129.
- [41] Dorigato A, Dzenis Y, Pegoretti A. Nanofiller Aggregation as Reinforcing Mechanism in Nanocomposites. *Procedia Engineering*. 2011;10:894-899.
- [42] Dorigato A, Dzenis Y, Pegoretti A. On the Reinforcement Mechanism in Particulate Nanocomposites. *Mechanics of Materials*. 2011; In press.
- [43] Dorigato A, Pegoretti A, Kolařík J. Nonlinear tensile creep of linear low density polyethylene/fumed silica nanocomposites: Time-strain superposition and creep prediction. *Polymer Composites*. 2010;31(11):1947-1955.
- [44] Jia Z, Luo Y, Guo B, Yang B, Du M, Jia D. Reinforcing and Flame-Retardant Effects of Halloysite Nanotubes on LLDPE. *Polymer-Plastics Technology and Engineering*. 2009;48(6):607-613.
- [45] Dorigato A, Pegoretti A. Fracture behaviour of linear low density polyethylene – fumed silica nanocomposites. *Engineering Fracture Mechanics*. 2012;79:213-224.
- [46] Franco-Urquiza E, Gamez Perez J, Sánchez-Soto M, Santana OO, MasPOCH ML. The effect of organo-modifier on the structure and properties of poly[ethylene-(vinyl alcohol)]/organo-modified montmorillonite composites. *Polymer International*. 2010;n/a-n/a.
- [47] MasPOCH ML, Franco-Urquiza E, Gamez-Perez J, Santana OO, Sánchez-Soto M. Fracture behaviour of poly[ethylene-(vinyl alcohol)]/organo-clay composites. *Polymer International*. 2009;58(6):648-655.
- [48] Bárány T, Czigány T, Karger-Kocsis J. Application of the essential work of fracture (EWF) concept for polymers, related blends and composites: A review. *Progress in Polymer Science*. 2010;35(10):1257-1287.
- [49] Pedrazzoli D, Ceccato R, Karger-Kocsis J, Pegoretti A. Viscoelastic behaviour and fracture toughness of linear-low-density polyethylene reinforced with synthetic boehmite alumina nanoparticles. *eXPRESS Polymer Letters*. 2013; Under submission.
- [50] Brandrup J, Immergut EH, Grulke EA. *Polymer Handbook* 1999.
- [51] Williams JG, Rink M. The standardisation of the EWF test. *Engineering Fracture Mechanics*. 2007;74(7):1009-1017.
- [52] Shamsi MH, Luqman M, Basarir F, Kim J-S, Yoon T-H, Geckeler KE. Plasma-modified halloysite nanocomposites: effect of plasma modification on the structure and dynamic mechanical properties of halloysite-polystyrene nanocomposites. *Polymer International*. 2010;59(11):1492-1498.
- [53] Zhao M, Liu P. Halloysite nanotubes/polystyrene (HNTs/PS) nanocomposites via in situ bulk polymerization. *Journal of Thermal Analysis and Calorimetry*. 2008;94(1):103-107.
- [54] Frost RL, Locos OB, Kristof J, Klopogge JT. Infrared spectroscopic study of potassium and cesium acetate-intercalated kaolinites. *Vibrational Spectroscopy*. 2001;26:33-42.

- [55] Abdel-Goad M, Pötschke P. Rheological characterization of melt processed polycarbonate-multiwalled carbon nanotube composites. *Journal of Non-Newtonian Fluid Mechanics*. 2005;128(1):2-6.
- [56] Cassagnau P. Melt rheology of organoclay and fumed silica nanocomposites. *Polymer*. 2008;49(9):2183-2196.
- [57] Ganß M, Satapathy BK, Thunga M, Weidisch R, Pötschke P, Jehnichen D. Structural interpretations of deformation and fracture behavior of polypropylene/multi-walled carbon nanotube composites. *Acta Materialia*. 2008;56(10):2247-2261.
- [58] Renger C, Kuschel P, Kristoffersson A, Clauss B, Oppermann W, Sigmund W. Rheology studies on highly filled nano-zirconia suspensions. *Journal of the European Ceramic Society*. 2007;27(6):2361-2367.
- [59] Sarvestani AS. Modeling the solid-like behavior of entangled polymer nanocomposites at low frequency regimes. *European Polymer Journal*. 2008;44(2):263-269.
- [60] Sepehr M, Utracki LA, Zheng X, Wilkie CA. Polystyrenes with macro-intercalated organoclay. Part II. Rheology and mechanical performance. *Polymer*. 2005;46(25):11569-11581.
- [61] Wu D, Wu L, Wu L, Zhang M. Rheology and thermal stability of polylactide/clay nanocomposites. *Polymer Degradation and Stability*. 2006;91(12):3149-3155.
- [62] Khumalo VM, Karger-Kocsis J, Thomann R. Polyethylene/synthetic boehmite alumina nanocomposites: Structure, thermal and rheological properties. *eXPRESS Polymer Letters*. 2010;4(5):264-274.
- [63] Liu M, Guo B, Du M, Chen F, Jia D. Halloysite nanotubes as a novel β -nucleating agent for isotactic polypropylene. *Polymer*. 2009;50(13):3022-3030.
- [64] Du M, Guo B, Jia D. Thermal stability and flame retardant effects of halloysite nanotubes on poly(propylene). *European Polymer Journal*. 2006;42(6):1362-1369.
- [65] Dorigato A, Pegoretti A, Frache A. Thermal stability of high density polyethylene-fumed silica nanocomposites. *Journal of Thermal Analysis and Calorimetry*. 2012;109(2):863-873.
- [66] Dzenis Y. Effect of aggregation of a dispersed rigid filler on the elastic characteristics of a polymer composite. *Mechanics of Composite Materials* 1986;22:14-22.
- [67] Lourenço MP, de Oliveira C, Oliveira AF, Guimarães L, Duarte HA. Structural, Electronic, and Mechanical Properties of Single-Walled Chrysotile Nanotube Models. *The Journal of Physical Chemistry C*. 2012;116(17):9405-9411.
- [68] Guimarães L, Enyashin AN, Seifert G, Duarte HIA. Structural, Electronic, and Mechanical Properties of Single-Walled Halloysite Nanotube Models. *The Journal of Physical Chemistry C*. 2010;114(26):11358-11363.
- [69] Du M, Guo B, Jia D. Newly emerging applications of halloysite nanotubes: a review. *Polymer International*. 2010;n/a-n/a.
- [70] Kolarik J, Pegoretti A. Non-linear tensile creep of polypropylene: Time-strain superposition and creep prediction. *Polymer*. 2006;47(1):346-356.
- [71] Yang W, Xie B-H, Shi W, Li Z-M, Liu Z-Y, Chen J, et al. Essential work of fracture evaluation of fracture behavior of glass bead filled linear low-density polyethylene. *Journal of Applied Polymer Science*. 2006;99(4):1781-1787.
- [72] Liu C. Enhancement of mechanical properties of poly(vinyl chloride) with polymethyl methacrylate-grafted halloysite nanotube. *Express Polymer Letters*. 2011;5(7):591-603.
- [73] Lin Y, Ng KM, Chan CM, Sun G, Wu J. High-impact polystyrene/halloysite nanocomposites prepared by emulsion polymerization using sodium dodecyl sulfate as surfactant. *Journal of colloid and interface science*. 2011;358(2):423-429.

[74] Oyama HT. Super-tough poly(lactic acid) materials: Reactive blending with ethylene copolymer. *Polymer*. 2009;50(3):747-751.

[75] Brunauer S, Emmett PH, E T. Adsorption of gases in multimolecular layers. Bureau of Chemistry and Soils and George Washington University. 1938;60:309-319.

Figure captions

Figure 1. TEM micrographs of (a) uHNT and (b) tHNT.

Figure 2. SEM images of the cryocut surfaces of (a) LLDPE-tHNT-4 and (b) LLDPE-tHNT-8.

Figure 3. TEM micrographs of the cryocut surfaces of (a) LLDPE-tHNT-4 and (b) LLDPE-tHNT-8 nanocomposites.

Figure 4. XRD traces of (a) HNT nanopowders, and (b) LLDPE and its HNT nanocomposites .

Figure 5. FTIR spectra of (a) HNT nanopowders, and (b) LLDPE and its HNT nanocomposites.

Figure 6. Complex viscosity $|\eta^*|$ and storage modulus (G') as a function of angular frequency (ω) for (a) LLDPE and LLDPE-HNT-4 nanocomposites and (b) LLDPE and LLDPE-HNT-8 nanocomposites.

Figure 7. Relative elastic modulus (E_C/E_M , where C and M subscripts refer to the composite and matrix, respectively) of LLDPE-HNT nanocomposites as a function of the filler volume content (V). Fitting of experimental data according to the model proposed by Dorigato et al. [41] (continuous line). Note that the error bars of experimental data are not given for sake of clarity.

Figure 8. Creep compliance ($D(t)$) of LLDPE and relative nanocomposites as a function of time ($T=30\text{ }^\circ\text{C}$, $\sigma_0 = 1\text{ MPa}$).

Figure 9. DMA properties of LLDPE and its HNT nanocomposites ($f = 1\text{ Hz}$): (a) Storage modulus (E') and (b) Loss tangent ($tg(\delta)$) as a function of temperature.

Figure 10. Serial photographs taken from the DEN-T specimens of the nanocomposites (A) LLDPE-tHNT-8 and (B) LLDPE-uHNT-8 during the EWF tests at different times.

Table 1. Physical properties of HNTs utilized in this work.

Filler	Density ^a [g·cm⁻³]	BET surface area ^b [m²·g⁻¹]	2θ₀₀₁ ^c [°] d₀₀₁ [nm]	2θ₀₂₀ ^c [°] d₀₂₀ [nm]	2θ₀₀₂ ^c [°] d₀₀₂ [nm]
uHNT	2.206 ± 0.001	31.3	13.26 0.667	20.43 0.434	24.71 0.360
tHNT	1.700 ± 0.001	61.8	12.41 0.713	20.29 0.437	24.90 0.357

^a Measurements were performed by using a Micromeritics AccuPyc[®] 1330 helium pycnometer (T = 23 °C).

^b Brunauer-Emett-Teller (BET) specific surface area [75].

^c Reflection (2 $\theta_{\square\square\square}$) and basal spacing (d_{hkl}) relative to XRD analyses.

Table 2. Melting and crystallization characteristics of LLDPE and relative nanocomposites from DSC measurements.

Sample	T_{m1} [°C]	$\square\Delta H_{m1}$ [J/g] (χ_{m1} [%])	T_c [°C]	ΔH_c [J/g] (χ_c [%])	T_{m2} [°C]	ΔH_{m2} [J/g] (χ_{m2} [%])
LLDPE	118.0	102.4 (35.3)	104.2	98.4 (33.9)	117.5	98.4 (33.9)
LLDPE-uHNT-1	117.8	101.3 (35.3)	105.5	101.0 (35.2)	117.7	100.3 (34.9)
LLDPE-uHNT-4	119.1	99.2 (35.6)	107.9	98.1 (35.2)	118.1	97.6 (35.1)
LLDPE-uHNT-8	119.1	96.5 (36.2)	107.1	94.9 (35.6)	117.9	94.0 (35.2)
LLDPE-tHNT-1	118.3	102.1 (35.6)	105.4	100.1 (34.9)	117.7	99.3 (34.6)
LLDPE-tHNT-4	118.2	99.5 (35.7)	108.2	97.9 (35.2)	117.9	97.2 (34.9)
LLDPE-tHNT-8	118.1	97.9 (36.7)	107.7	95.1 (35.6)	118.1	94.5 (35.4)

T_{m1} : Melting temperature recorded during the first heating scan.

ΔH_{m1} (χ_{m1}): Melting enthalpy and normalized crystallinity recorded during the first heating scan.

T_c : Crystallization peak temperature.

ΔH_c (χ_c): Crystallization enthalpy and normalized crystallinity.

T_{m2} : Melting temperature recorded during the second heating scan.

ΔH_{m2} (χ_{m2}): Melting enthalpy and normalized crystallinity recorded during the second heating scan.

Table 3. TGA parameters of LLDPE and relative nanocomposites

Sample	T _{d, onset} [°C]	T _{d, max} [°C]	MMLR [mg °C ⁻¹]	Char [%]
LLDPE	457.0	477.1	0.195	0.3
LLDPE-uHNT-1	458.9	478.0	0.221	0.6
LLDPE-uHNT-4	461.5	478.2	0.243	2.6
LLDPE-uHNT-8	465.3	480.4	0.293	5.7
LLDPE-tHNT-1	458.5	480.8	0.236	0.4
LLDPE-tHNT-4	461.7	482.2	0.272	1.8
LLDPE-tHNT-8	465.7	484.2	0.308	5.0
uHNT	/	/	/	74.7
tHNT	/	/	/	57.9

T_{d, onset}: Onset degradation temperature.

T_{d, max}: Maximum degradation rate temperature.

MMLR: Maximum mass loss rate.

Char [%]: Residual weight percentage.

Table 4a. Quasi-static tensile properties at yield and at break.

Sample	Tensile modulus [MPa]	Tensile Strength at Yield [MPa]	Tensile Strength at Break [MPa]	Elongation at Break [%]	TEB _{qs} ^a [J/m ³]
LLDPE	200 ± 6	11.7 ± 0.2	21.6 ± 1.0	1390 ± 91	183.5 ± 14.1
LLDPE-uHNT-1	216 ± 13	11.2 ± 0.8	19.4 ± 0.8	1085 ± 58	172.1 ± 17.3
LLDPE-uHNT-4	248 ± 17	10.8 ± 0.4	13.7 ± 0.6	851 ± 74	160.5 ± 16.2
LLDPE-uHNT-8	322 ± 5	11.6 ± 0.4	13.8 ± 0.7	713 ± 26	151.2 ± 14.9
LLDPE-tHNT-1	220 ± 16	12.8 ± 0.2	21.0 ± 0.6	1157 ± 66	176.2 ± 15.2
LLDPE-tHNT-4	284 ± 24	13.8 ± 0.3	18.8 ± 0.4	1001 ± 19	173.5 ± 14.1
LLDPE-tHNT-8	388 ± 46	12.6 ± 0.3	18.9 ± 0.3	1017 ± 45	174.2 ± 16.3

^a Tensile energy to break measured during quasi-static tensile mechanical test.

Table 4b. Tensile impact properties at break.

Sample	Maximum Strength [MPa]	Elongation at Break [%]	TEB ^a [J/m ³]
LLDPE	40.2 ± 2.7	135 ± 15	18.9 ± 2.3
LLDPE-uHNT-1	40.0 ± 3.5	121 ± 13	18.0 ± 1.6
LLDPE-uHNT-4	39.3 ± 4.1	95 ± 16	15.2 ± 3.2
LLDPE-uHNT-8	35.3 ± 3.0	89 ± 11	14.4 ± 0.5
LLDPE-tHNT-1	40.2 ± 3.1	155 ± 12	19.4 ± 2.7
LLDPE-tHNT-4	40.8 ± 3.7	142 ± 10	19.3 ± 2.0
LLDPE-tHNT-8	38.2 ± 5.7	129 ± 13	18.7 ± 1.3

^a Tensile energy to break measured during tensile impact test.

Table 5. Creep compliance data and dynamic mechanical properties of LLDPE and relative nanocomposites (f = 1 Hz).

Sample	D_e [GPa ⁻¹]	$D_{ve,2000s}$ [GPa ⁻¹]	$D_{tot,2000s}$ [GPa ⁻¹]	$E' (-130\text{ }^\circ\text{C})$ [MPa]	$E' (23\text{ }^\circ\text{C})$ [MPa]	$E'' (23\text{ }^\circ\text{C})$ [MPa]	T_g [°C]
LLDPE	5.96	7.39	13.35	4236	416	26.0	-110.5
LLDPE-uHNT-1	5.85	7.33	13.18	4318	422	50.7	-110.9
LLDPE-uHNT-4	5.62	7.11	12.73	4724	539	56.1	-109.1
LLDPE-uHNT-8	5.55	6.72	12.27	4970	778	59.3	-109.2
LLDPE-tHNT-1	5.80	7.33	13.13	4358	518	49.5	-110.0
LLDPE-tHNT-4	5.56	4.52	10.08	4634	738	62.1	-109.9
LLDPE-tHNT-8	5.46	4.25	9.71	5094	813	66.8	-109.1

D_e : Elastic creep compliance.

$D_{ve,2000s}$: Viscoelastic creep compliance at 2000 s.

$D_{tot,2000s}$: Total creep compliance at 2000 s.

$E' (-130\text{ }^\circ\text{C})$: Storage modulus at -130 °C.

$E' (23\text{ }^\circ\text{C})$: Storage modulus at +23 °C.

$E'' (23\text{ }^\circ\text{C})$: Loss modulus at +23 °C.

T_g : Glass transition temperature as recorded in $tg\delta$ peak.

Table 6. Specific EWF properties of LLDPE and relative nanocomposites.

Sample	w_e [kJ / m ²]	βw_p [MJ / m ³]	β	$w_{e,y}$ [kJ / m ²]	$\beta' w_{p,y}$ [MJ / m ³]	$w_{e,n}$ [kJ / m ²]	$\beta'' w_{p,n}$ [MJ / m ³]
LLDPE	26.7 ± 3.6	12.7 ± 0.4 (0.983)	0.32 ± 0.04	2.7 ± 0.3	2.8 ± 0.1 (0.997)	24.2 ± 3.6	9.9 ± 0.4 (0.992)
LLDPE-uHNT-1	29.4 ± 3.4	12.0 ± 0.4 (0.984)	0.31 ± 0.03	3.3 ± 0.5	2.7 ± 0.1 (0.994)	26.1 ± 3.4	9.3 ± 0.4 (0.989)
LLDPE-uHNT-4	38.1 ± 1.9	8.7 ± 0.2 (0.990)	0.30 ± 0.04	6.6 ± 0.5	2.2 ± 0.1 (0.990)	31.5 ± 2.0	6.5 ± 0.2 (0.991)
LLDPE-uHNT-8	21.8 ± 2.3	12.2 ± 0.3 (0.992)	0.26 ± 0.05	8.8 ± 0.5	2.1 ± 0.1 (0.983)	13.0 ± 2.4	10.1 ± 0.3 (0.988)
LLDPE-tHNT-1	29.0 ± 3.0	12.9 ± 0.3 (0.988)	0.29 ± 0.06	3.7 ± 0.5	2.2 ± 0.1 (0.986)	25.3 ± 3.0	10.7 ± 0.3 (0.990)
LLDPE-tHNT-4	40.4 ± 3.0	10.9 ± 0.3 (0.984)	0.25 ± 0.05	6.4 ± 0.7	1.8 ± 0.1 (0.964)	34.0 ± 3.1	9.1 ± 0.3 (0.991)
LLDPE-tHNT-8	55.0 ± 1.3	6.4 ± 0.2 (0.992)	0.26 ± 0.03	6.5 ± 0.4	1.6 ± 0.1 (0.986)	48.5 ± 1.4	4.8 ± 0.2 (0.988)

w_e : Specific essential work of fracture.

βw_p : Specific non-essential work of fracture.

β : Shape factor (taking into account an elliptical shape of the plastic zone).

$w_{e,y}$: Specific essential work of fracture of yielding.

$\beta' w_{p,y}$: Specific non-essential work of fracture of yielding.

$w_{e,n}$: Specific essential work of fracture of necking.

$\beta'' w_{p,n}$: Specific non-essential work of fracture of necking.

(The values in brackets correspond to R² values obtained from the linear regression of the data)

Figure 1
(1-column fitting image)

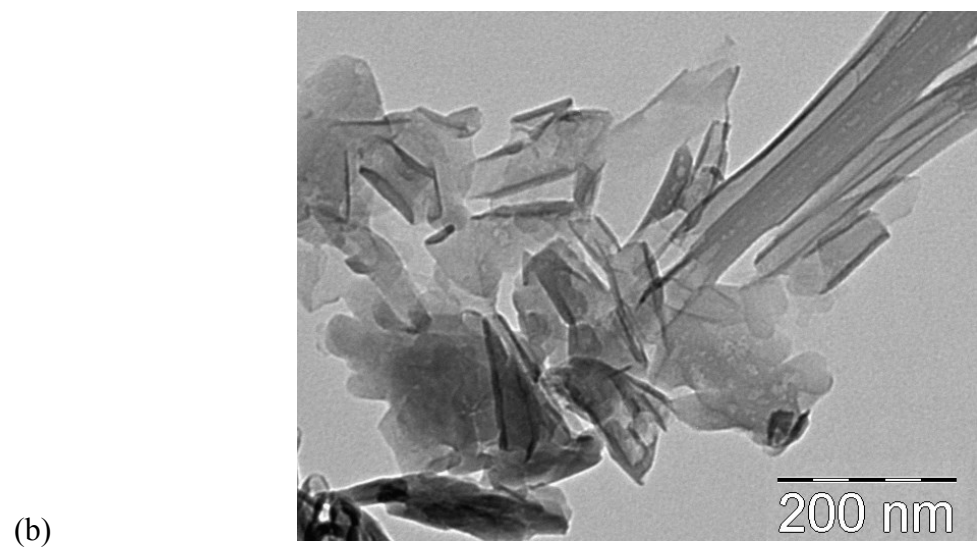
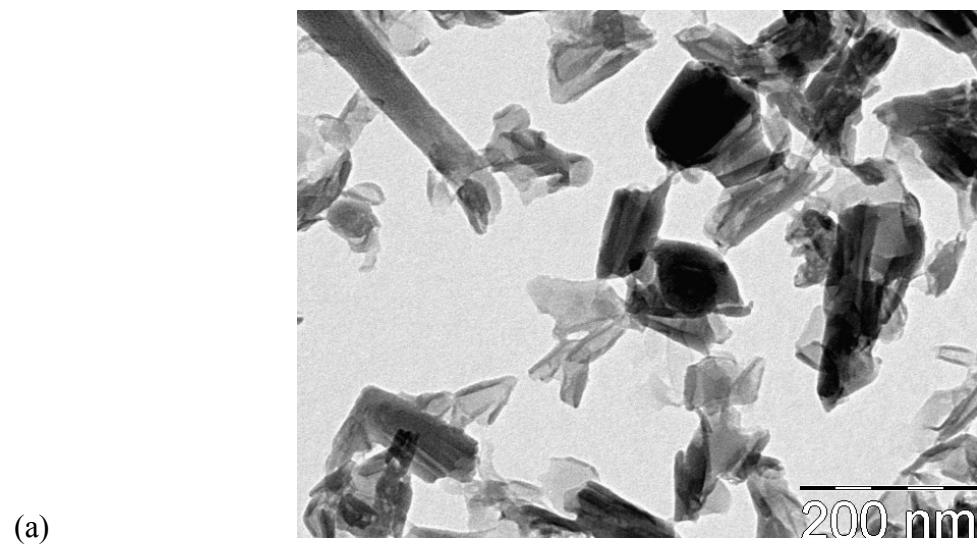
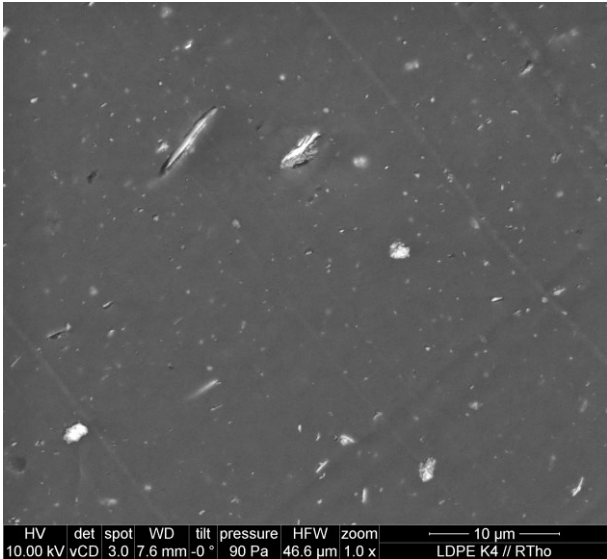


Figure 2
(1-column fitting image)

(a)



(b)

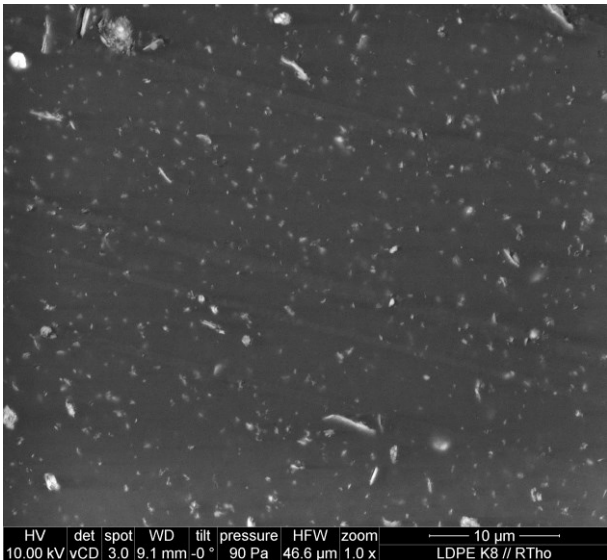


Figure 3
(1-column fitting image)

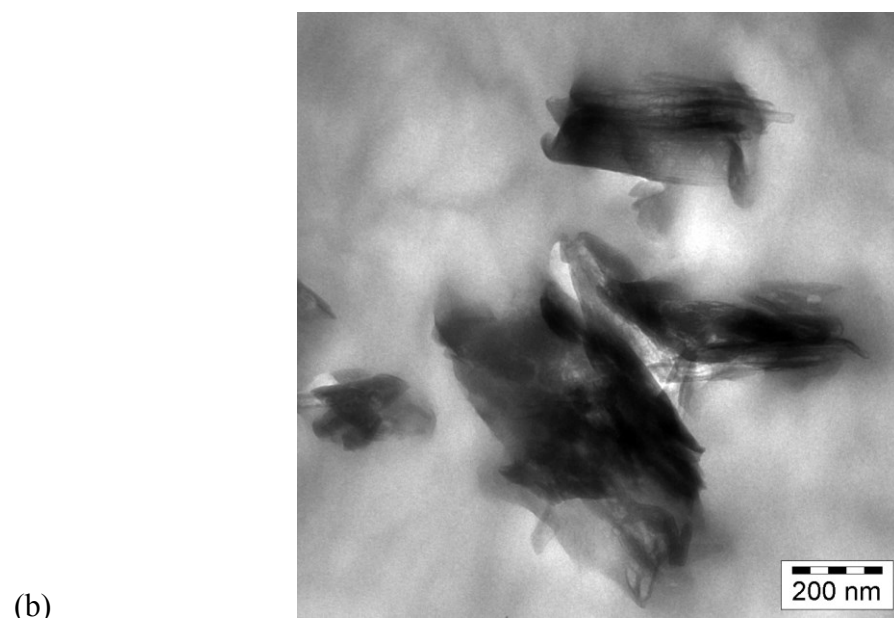
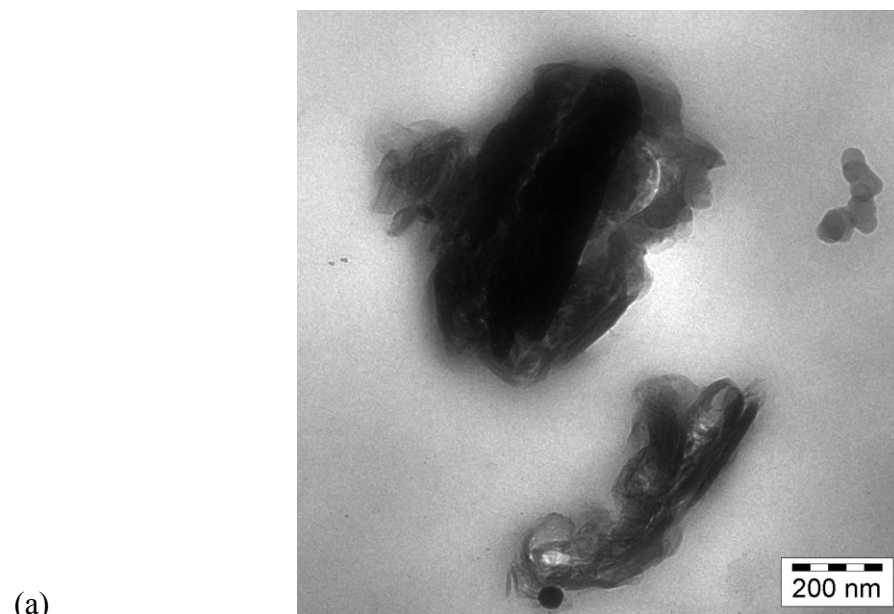
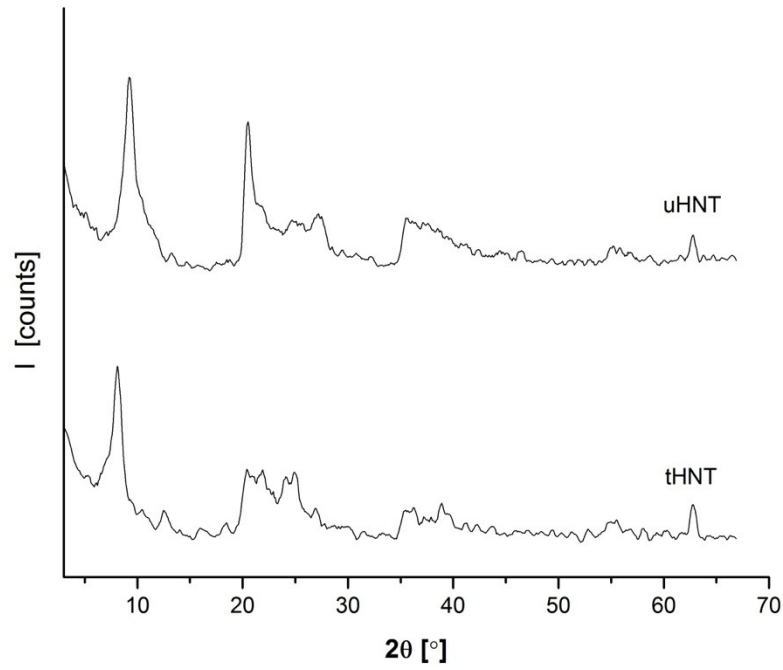
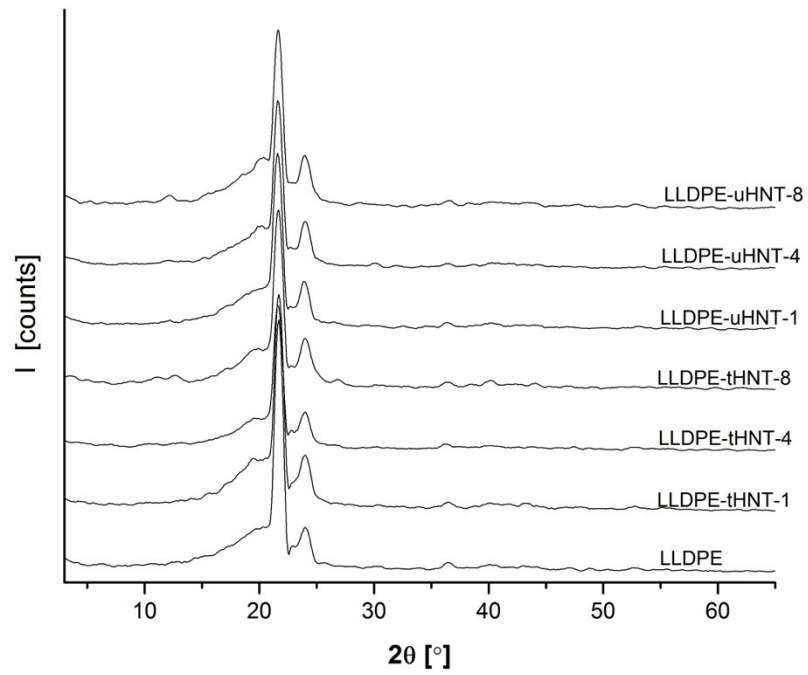


Figure 4
(1-column fitting image)

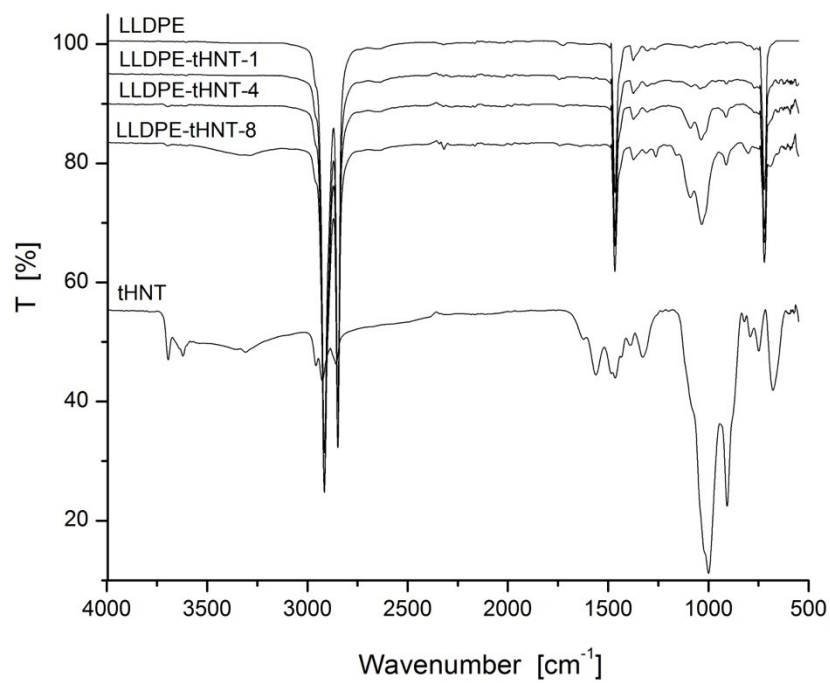


(a)

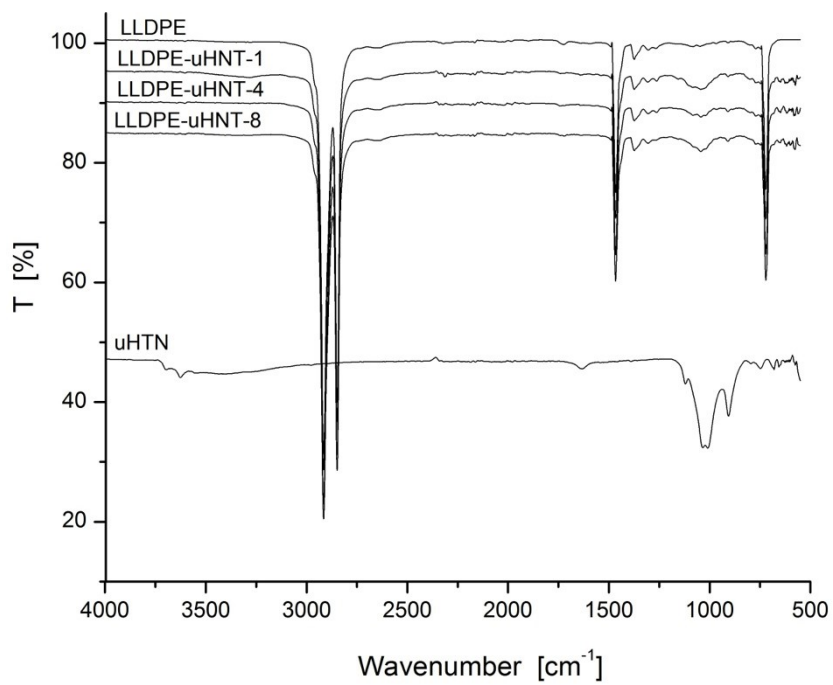


(b)

Figure 5
(1-column fitting image)

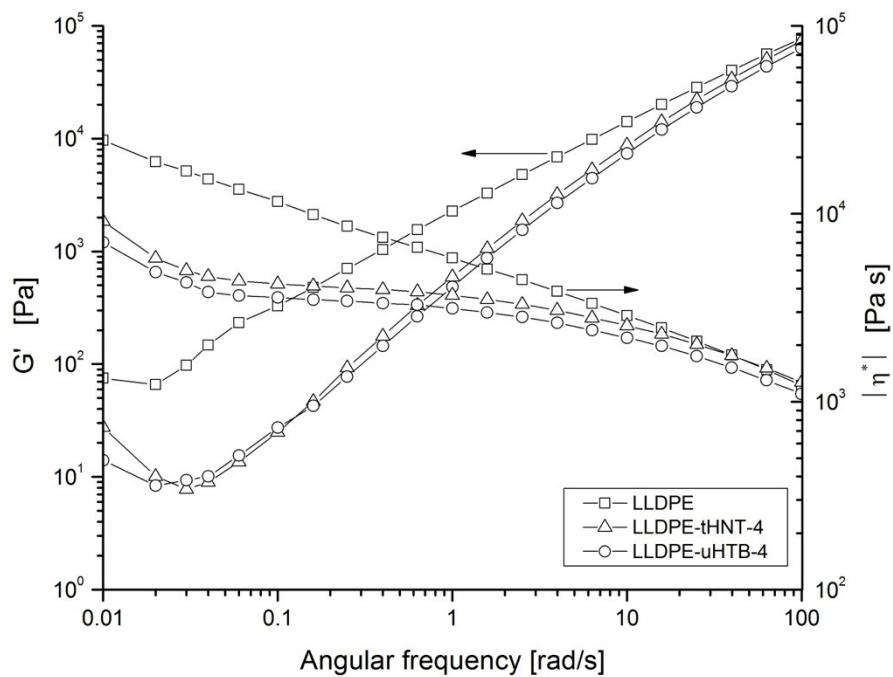


(a)

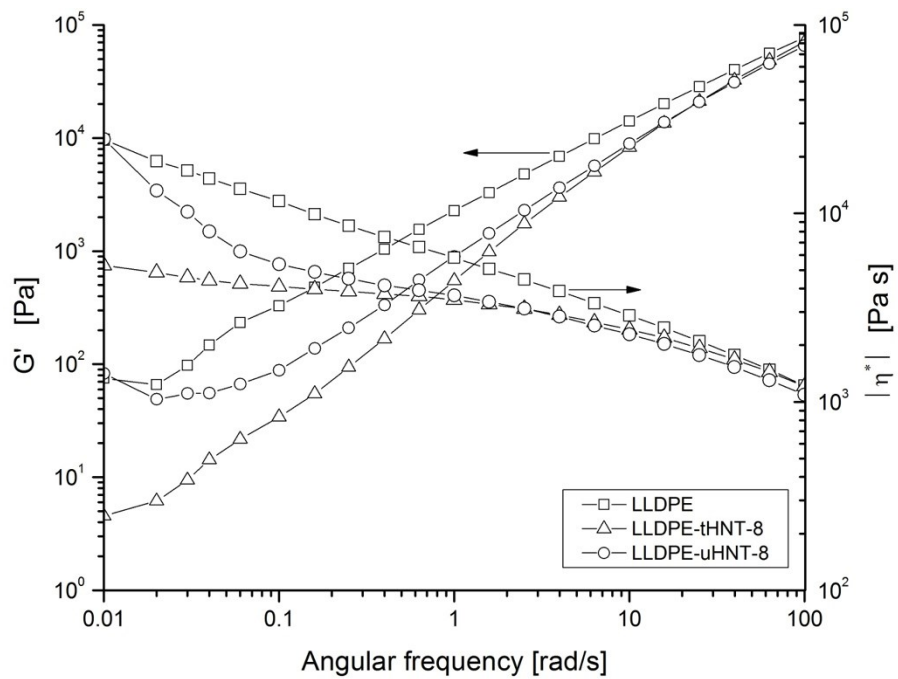


(b)

Figure 6
(1-column fitting image)



(a)



(b)

Figure 7
(1-column fitting image)

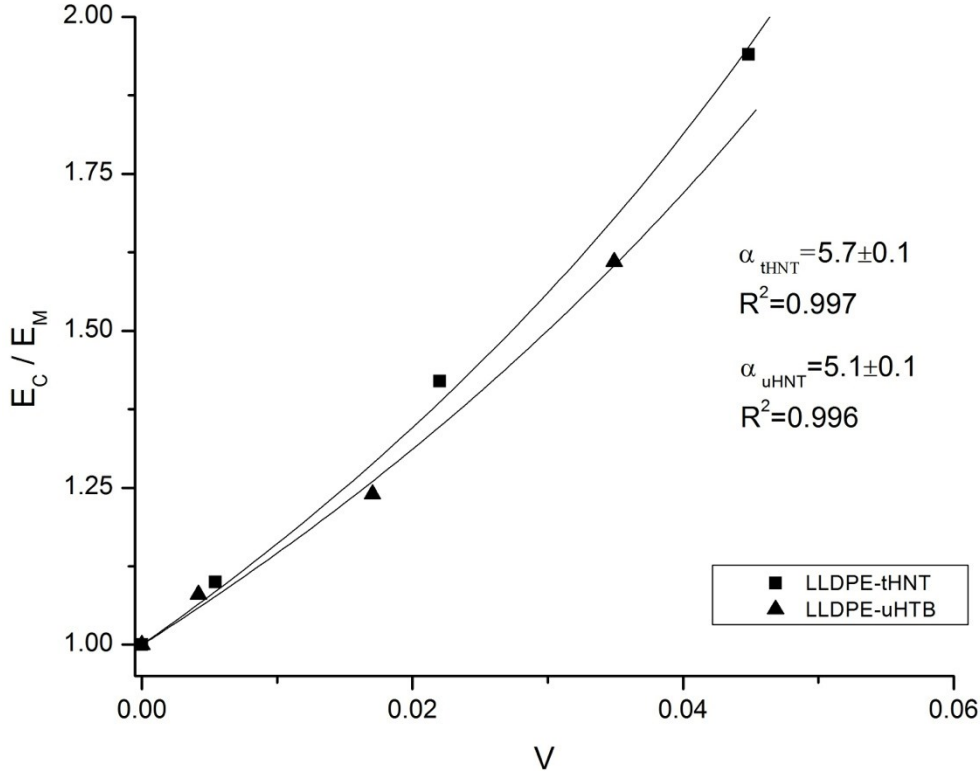


Figure 8
(1-column fitting image)

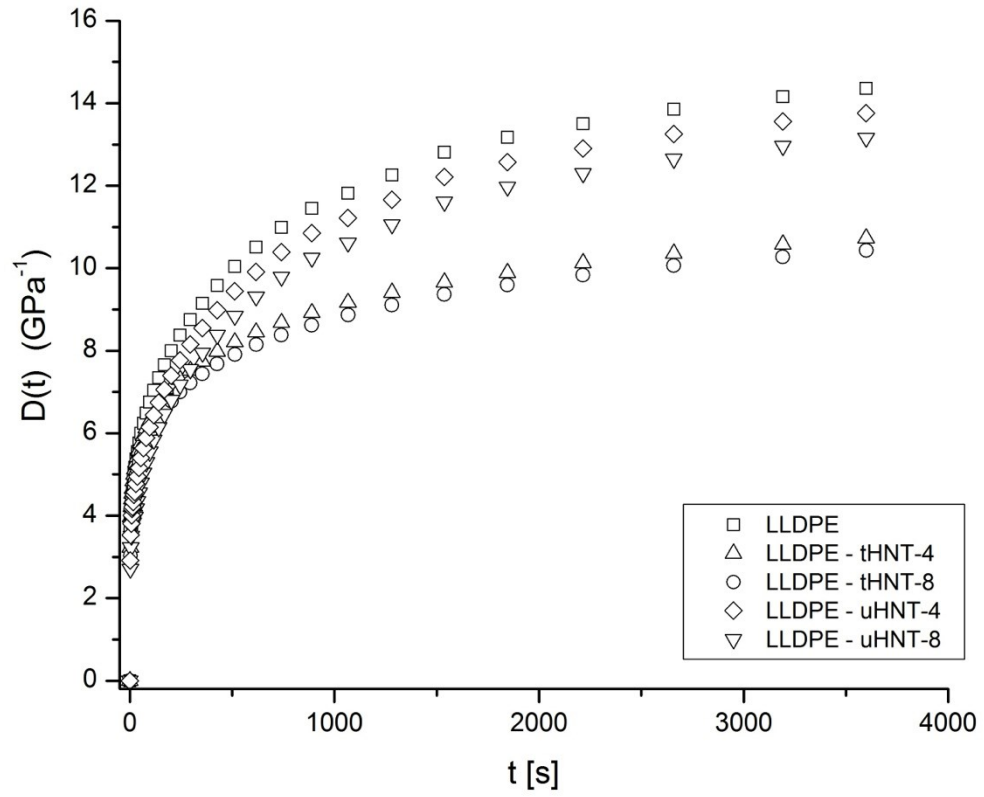
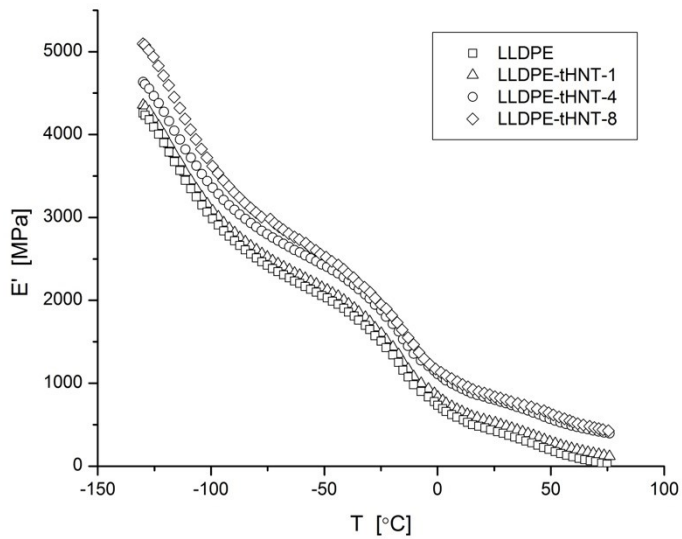
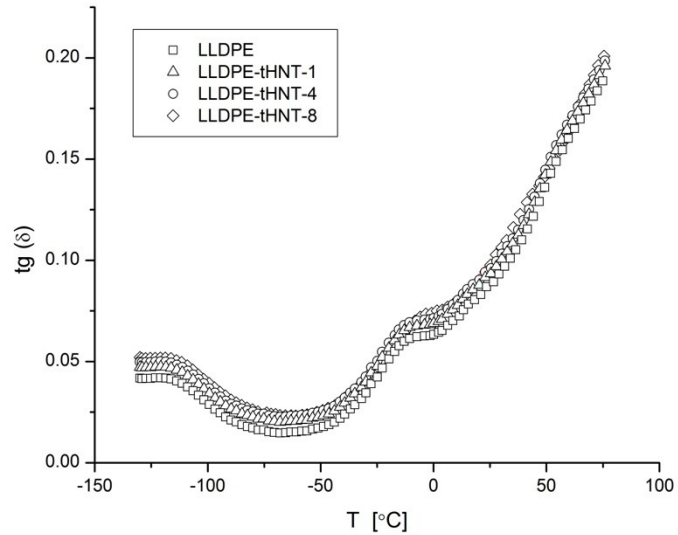


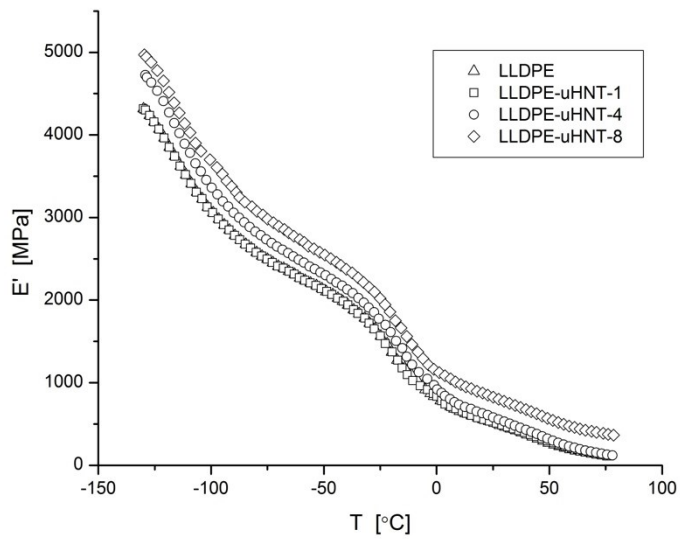
Figure 9
(2-column fitting image)



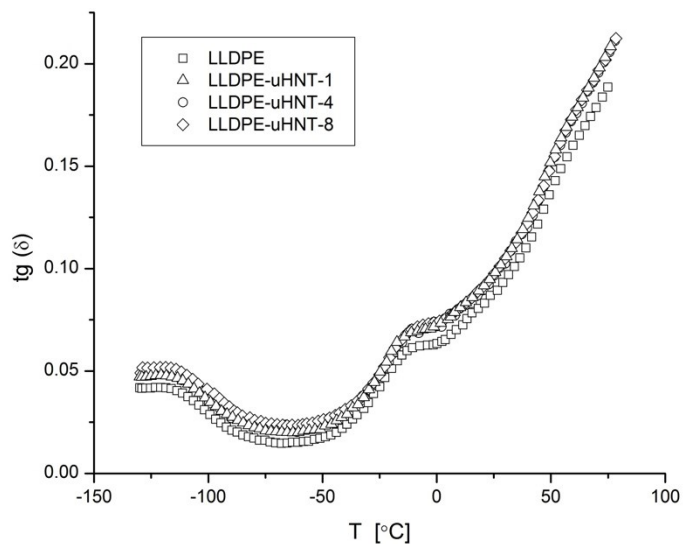
(a)



(c)

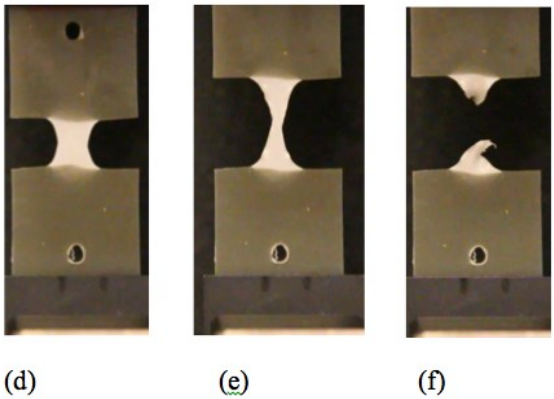
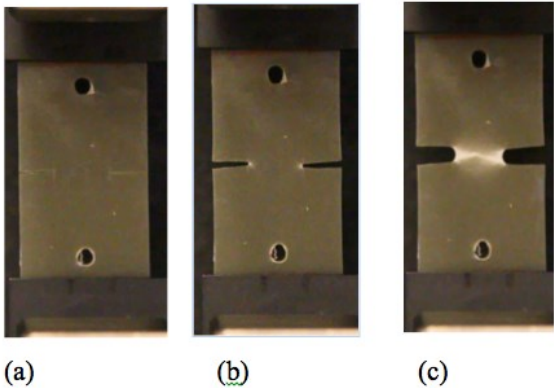


(b)

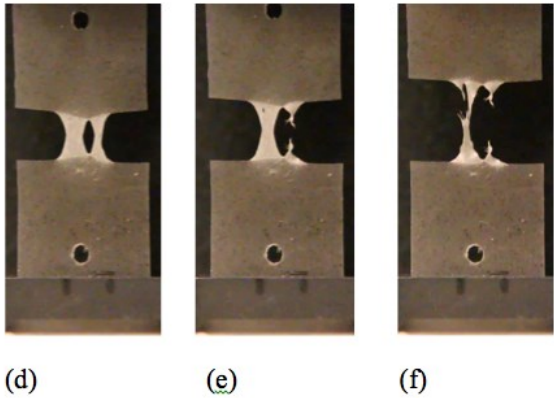
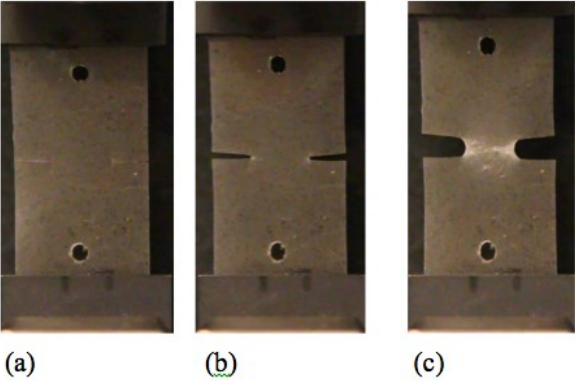


(d)

Figure 10
(2-column fitting image)



(A)



(B)